Numerical Investigation of the Nozzle Plume Interaction in Hypersonic Flow

Axel Buck[1], Christian Mundt[2]

Abstract

During flight of propelled hypersonic vehicles, a strong interaction between the hypersonic flow around the vehicle and the nozzle exhaust plume takes place. The interaction affects the entire structure of the flow behind of the vehicle, altering both aerodynamic performance and stability. Generic slender vehicle geometries with and without a propulsion element were analyzed numerically in this study. A nozzle configuration that is flush with the vehicle rear shows a stable plume structure in hypersonic flight, but experiences transient flow separation at low supersonic flight. A configuration with a protruding nozzle element shows a large separation outside of the nozzle with unsteady separation for laminar flow. It also shows a backward shift in the pressure center, strongly increasing the longitudinal stability of the vehicle.

Keywords: *hypersonics, nozzle plume*

Nomenclature

Latin

A – Area
D – Diffusion coefficient
E – Total energy
M – Molar mass
Ma – Mach number
T – Temperature
$\boldsymbol{W}$ – State vector
Y – Species mass fraction
c_p – Isobaric specific heat
$\boldsymbol{f}$ – Flux vector
h – Enthalpy
k – Turbulent kinetic energy
p – Pressure
q – Conductive heat flux

t – Time
u, v, w – x, y, z-Velocity components
x, y, z – Spacial directions

Greek

γ – Ratio of specific heats
ϵ – Expansion area ratio
λ – Thermal conductivity
ρ – Density
τ – Shear stress
$\dot{\Omega}$ – Net mass production
ω – Turbulent dissipation rate

Subscripts

0 – Stagnation condition
∞ – Freestream condition

1. Introudction

In propelled hypersonic flight, the vehicle performance is strongly affected by the flow structure of the nozzle. The stability of the nozzle flow can change drastically depending on its operating conditions, mainly the atmospheric pressure. For overexpanded jets major instabilities have been observed depending on the back-pressure, a literature survey can be found in [1]. Most of these investigations are done for nozzle jet expansion into stationary external fluid, e.g. [2]. Some experiments and numerical work was done for supersonic external flow, e.g. [3, 4] and hypersonic external flow at lower Reynolds numbers [5, 6]. So in this paper a numerical investigation is performed on the interaction of a rocket

---
[1]*Universität der Bundeswehr München, Faculty of Aerospace Engineering, Institute of Thermodynamics, Werner-Heisenberg-Weg 39, 85577 Neubiberg (Germany), axel.buck@unibw.de*

[2]*Universität der Bundeswehr München, Faculty of Aerospace Engineering, Institute of Thermodynamics, Werner-Heisenberg-Weg 39, 85577 Neubiberg (Germany), christian.mundt@unibw.de*

nozzle plume in hypersonic flow. Specifically, the hypersonic flow at high ambient pressure conditions around a propelled slender vehicle was investigated numerically.

2. Numerical simulation technique

The numerical investigations in this publication were conducted by 3D CFD (Computational Fluid Dynamics) simulations. The semi-commercial Navier-Stokes solver NSMB (Navier-Stokes-Multi-Block) [7] was used. NSMB uses block-structured meshes with hexagonal cells. It is designed to be run in parallel on computing clusters; the OpenMPI library is used as message passing interface.

2.1. Discretization of Navier-Stokes equations

NSMB is a full-3D density-based Navier-Stokes solver, which uses the finite-volume approximation. The Navier-Stokes equations can be written in the following conservation form, Einstein summation convention is applied:

$$\frac{\partial}{\partial t}\left(\boldsymbol{W}\right) + \frac{\partial}{\partial x_i}\left(\boldsymbol{f_i} - \boldsymbol{f_{v,i}}\right) = 0 \tag{1}$$

For modeling turbulence with Reynolds-averaged Navier-Stokes (RANS) models, Favre-averaging is applied to the Navier-Stokes equations, which yields the following expression for the state vector $\boldsymbol{W}$, the inviscid fluxes $\boldsymbol{f_i}$, and the viscous fluxes $\boldsymbol{f_{v,i}}$ in the mean flow.

$$W = \left(\bar{\rho}, \bar{\rho}\tilde{u}, \bar{\rho}\tilde{v}, \bar{\rho}\tilde{w}, \bar{\rho}\tilde{E}\right)^T \tag{2}$$

$$\boldsymbol{f_1} = \begin{pmatrix} \bar{\rho}\tilde{u} \\ \bar{\rho}\tilde{u}^2 + \bar{p} \\ \bar{\rho}\tilde{u}\tilde{v} \\ \bar{\rho}\tilde{u}\tilde{w} \\ \tilde{u}\left(\bar{\rho}\tilde{E} + \bar{p}\right) \end{pmatrix}, \boldsymbol{f_2} = \begin{pmatrix} \bar{\rho}\tilde{v} \\ \bar{\rho}\tilde{v}\tilde{u} \\ \bar{\rho}\tilde{v}^2 + \bar{p} \\ \bar{\rho}\tilde{v}\tilde{w} \\ \tilde{v}\left(\bar{\rho}\tilde{E} + \bar{p}\right) \end{pmatrix}, \boldsymbol{f_3} = \begin{pmatrix} \bar{\rho}\tilde{w} \\ \bar{\rho}\tilde{w}\tilde{u} \\ \bar{\rho}\tilde{w}\tilde{v} \\ \bar{\rho}\tilde{w}^2 + \bar{p} \\ \tilde{w}\left(\bar{\rho}\tilde{E} + \bar{p}\right) \end{pmatrix} \tag{3}$$

$$\boldsymbol{f_{v,1}} = \begin{pmatrix} 0 \\ \tau_{xx} - \overline{\rho u'u'} \\ \tau_{xy} - \overline{\rho u'v'} \\ \tau_{xz} - \overline{\rho u'w'} \\ \left(\tau\tilde{U}\right)_x - q_x - \sigma_{k,x} \end{pmatrix}, \boldsymbol{f_{v,2}} = \begin{pmatrix} 0 \\ \tau_{yx} - \overline{\rho v'u'} \\ \tau_{yy} - \overline{\rho v'v'} \\ \tau_{yz} - \overline{\rho v'w'} \\ \left(\tau\tilde{V}\right)_y - q_y - \sigma_{k,y} \end{pmatrix}, \boldsymbol{f_{v,3}} = \begin{pmatrix} 0 \\ \tau_{wx} - \overline{\rho w'u'} \\ \tau_{wy} - \overline{\rho w'v'} \\ \tau_{wz} - \overline{\rho w'w'} \\ \left(\tau\tilde{W}\right)_z - q_z - \sigma_{k,z} \end{pmatrix} \tag{4}$$

Here, $\bar{\phi} = 1/T \int_T \phi(t)dt$ denotes the Reynolds-averaged value and $\tilde{\phi} = \overline{\rho\phi}/\bar{\rho}$ describes the Favre-average. τ_{ij} is the laminar shear stress, $\overline{\rho u'_i u'_j}$ are the Reynolds stress terms, $(\tau\tilde{U}_i)_i$ is the laminar viscous dissipation, and $\sigma_{k,i}$ is the turbulent dissipation term. $q_i = -(\lambda + \lambda_T) \, \partial T/\partial x_i$ is the conductive heat flux; the turbulent conductivity λ_T is computed from the eddy viscosity using an eddy diffusivity approach.

The turbulent terms were modeled with the Wilcox k-ω two-equation model in its low-Reynolds form [8]. The Navier-Stokes equations (1) are appended by conservation equations for the turbulent kinetic energy k and the specific dissipation rate ω. The Reynolds stress tensor is then reconstructed using the Boussinesq hypothesis. The model was chosen because of its good performance in similar conditions in a previous study [9].

The inviscid fluxes are discretized in space with a second-order accurate AUSM+ scheme [10], while the viscous fluxes are handled with a central scheme. For steady-state simulations, the equations are advanced in time with an implicit scheme using local time-stepping. The resulting set of linear equations is solved approximately each timestep with the LU-SGS method (Lower-Upper Symmetric-Gauss-Seidel) [11]. For unsteady calculations, an explicit three-stage Runge-Kutta scheme is applied [12].

2.2. Chemical Modelling

To include chemical reactions in the numerical model, the Navier-Stokes equations (1) are appended with one additional conservation equation for each participating species s:

$$\frac{\partial}{\partial t}\left(\rho_s\right) + \frac{\partial}{\partial x_i}\left(\rho_s u_i - \rho D \frac{\partial Y s}{\partial x_i}\right) = \dot{\Omega}_s \tag{5}$$

ρ_s and Y_s are the partial density and the mass fraction of species s. $\dot{\Omega}_s$ is the net mass production of species s, D is its diffusion coefficient, and h_s is its enthalpy.

A chemical energy flux term $f_{e,i}$ is then added to the viscous energy flux in equation (4):

$$f_{e,i} = \rho \sum_s h_s D \frac{\partial Y_s}{\partial x_i} \tag{6}$$

For modeling chemical reactions in NSMB, the open source library Mutation++ was used [13]. It provides efficient algorithms for simulating chemically reacting flows and was used to compute the mixture composition and its thermodynamic and transport properties at each timestep.

For the present simulations, chemical reactions in the external flow were included using a 5 species model for air including O_2, N_2, O, N, and NO. Chemical reactions were modeled with a laminar finite rate chemistry model using Arrhenius expressions. The included chemical reactions can be seen in equations (7) to (10), where M is one of the other participating species, the reaction rate coefficients can be found in [14].

$$N_2 + M \rightleftharpoons 2N + M \tag{7}$$
$$O_2 + M \rightleftharpoons 2O + M \tag{8}$$
$$N_2 + O \rightleftharpoons NO + N \tag{9}$$
$$NO + O \rightleftharpoons O_2 + N \tag{10}$$

In order to analyze the gas dynamic effects in and around the nozzle plume, it is desirable to include the different fluid properties of the external flow and the nozzle exhaust flow in the numerical model. In typical hypersonic applications, solid rocket motors are used. The propellant is often a composite material that consists of a combination of ammonium perchlorate, aluminum, and a polymer binder [15]. The resulting exhaust gas is a mixture of a large number of reaction products (often more than 20). An accurate representation of the flow would require the definition of a very complex reaction mechanism and the inclusion of many additional conservation equations. The computational effort for such a numerical model is outside of the scope of this publication.

Fig. 1a shows the ratio of specific heats γ of such a propellant at chemical equilibrium in a relevant density and temperature range. The data was produced with the NASA CEA (Chemical Equilibrium with Applications) program [16]. γ shows very little variation in most of the input range. Larger variations in γ are observed at the lower end of the temperature spectrum at $T \approx 300\ \mathrm{K}$ and for high temperature, low density conditions. Fig. 1b shows the temperature in the core of the exhaust plume along the axis, using the ideal gas assumption for the nozzle gas. The minimum temperature in the simulated domain is $T \approx 1000\ \mathrm{K}$, hence the temperature regions, where γ is not constant are not relevant for the investigated cases. Reactions in the exhaust gas were therefore neglected in this publication to decrease the computational effort. The nozzle exhaust gas was modeled as a perfect gas with a constant molar Mass of $M = 26\ \mathrm{g/mol}$ and a ratio of specific heats $\gamma = 1.2$. This reduced the computational effort significantly, while still including the high-temperature effects in the external flow.

The viscosity in the entire domain was modeled with the Sutherland model for viscosity and the diffusion coefficient was calculated from a constant Lewis number of $\mathrm{Le} = \lambda/(\rho D c_p) = 1.2$. At the freestream unit Reynolds number of $\mathrm{Re}_\infty = (\rho_\infty U_\infty)/\mu_\infty = 1.75 \times 10^8\ \mathrm{1/m}$ at $\mathrm{Ma}_\infty = 7$, both viscous and diffusive processes have a minor effect compared to inertial processes. Neglecting the influence of the mixture on the transport coefficients is therefore justified.
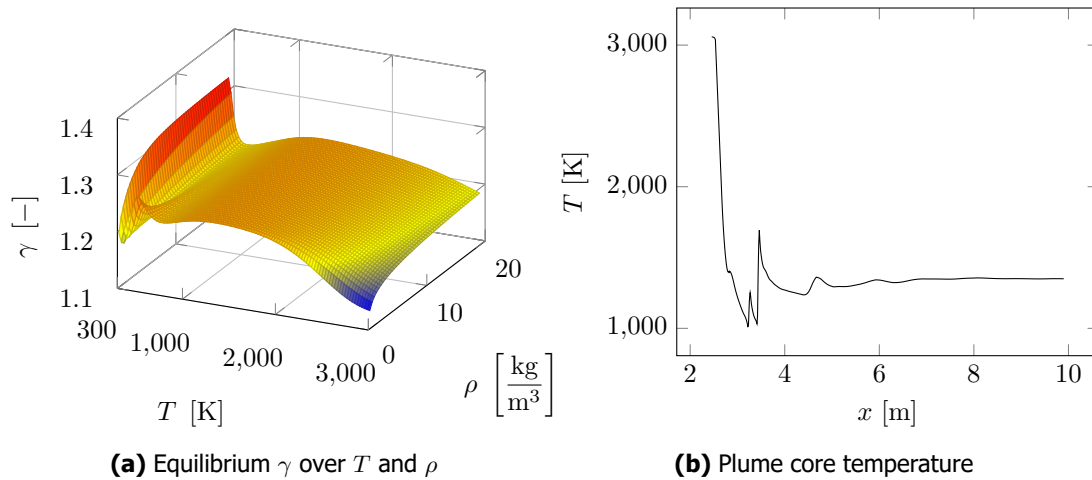
(a) Equilibrium γ over T and ρ

(b) Plume core temperature

Fig 1. Thermodynamic behavior of the nozzle plume. a) ratio of specific heats γ at chemical equilibrium in the exhaust gas for a range of temperatures and densities. b) plume core temperature distribution along the axis for the ideal gas assumption.
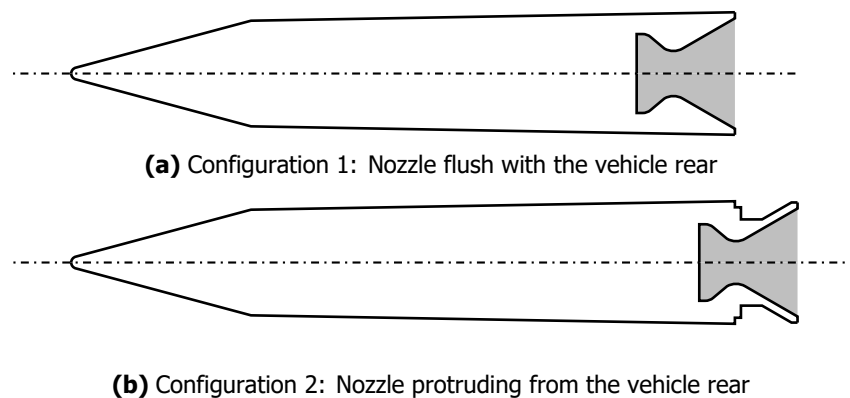

(a) Configuration 1: Nozzle flush with the vehicle rear

(b) Configuration 2: Nozzle protruding from the vehicle rear

Fig 2. Schematic view of the two simulated geometries, both use the same internal nozzle geometry and the same vehicle forebody.

3. Physical setup

A generic slender hypersonic vehicle was simulated in this paper. The configuration consists of a spherical nose with a $r = 7\ \mathrm{mm}$ radius and two adjoining conical sections with half angles of $\phi = 8\ °$ and $\phi = 1.12\ °$. A de Laval nozzle with an area ratio of $\epsilon = {}^{A_e}/A^* \approx 3.46$ is positioned in the rear of the vehicle.

Two main propelled configurations were investigated, see fig. 2. The geometry of the forebody and the internal nozzle walls are equal, only the axial position of the nozzle is altered between configurations. The nozzle element is flush with the vehicle rear in configuration 1. Configuration 2 has a protruding nozzle element, which effectively creates a cavity followed by a conical ramp along the outside of the nozzle.

To evaluate the plume interaction in a high thermal and mechanical load case, the free-stream conditions were $p_\infty = 101350\ \mathrm{Pa}$, $T_\infty = 273.15\ \mathrm{K}$ at Mach numbers from $\mathrm{Ma}_\infty = 1.3$ to $\mathrm{Ma}_\infty = 7$ resulting in unit Reynolds numbers from $\mathrm{Re}_\infty = 3.25 \times 10^7\ {}^1/\mathrm{m}$ to $\mathrm{Re}_\infty = 1.75 \times 10^8\ {}^1/\mathrm{m}$. To improve convergence and reduce the numerical dissipation in the applied shock-capturing scheme, the mesh was refined in the vicinity of the bow shock. The shape of the bow shock was estimated by the empirical correlation
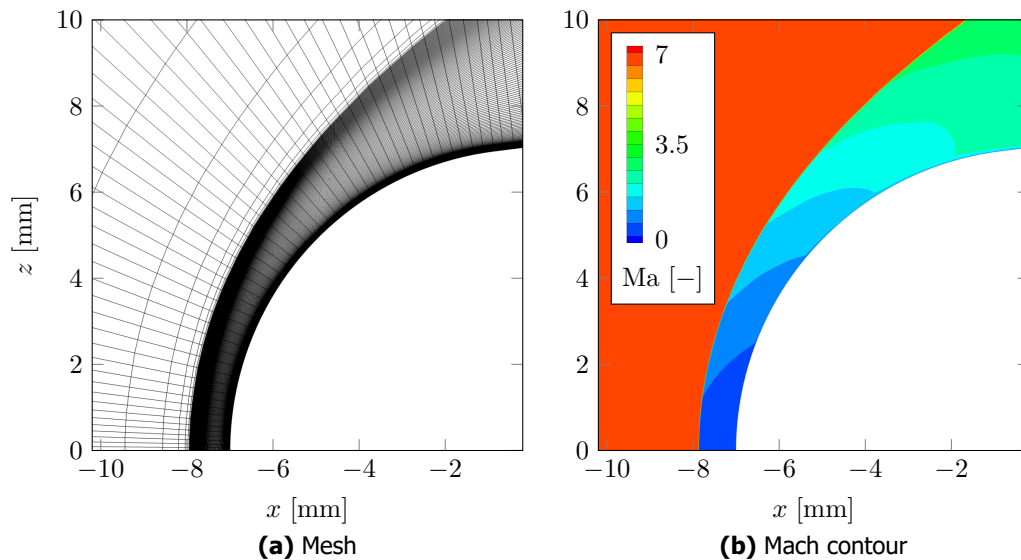
(a) Mesh

(b) Mach contour

Fig 3. Nose of the modeled vehicle, the coordinate origin is in the center of the nose. (a) shows the mesh around the nose. Note the refinement near the wall and around the estimated shock contour. (b) shows a Mach number contour plot of the nose region at $\mathrm{Ma}_\infty = 7$.

by Klaimon [17] and the outer edge of the inflow boundary was generated parallel to the expected shape. The mesh was then adapted automatically to the shock shape, which was determined using a Mach number threshold along wall-normal grid lines. Because NSMB uses block-structured grids, general shock adaption of internal shocks is very difficult, so only the outer bow shock was adapted.

Fig. 3a shows the mesh around the vehicle nose after the mesh adaption and a Mach number plot for $\mathrm{Ma}_\infty = 7$ is shown in fig. 3b. The algorithm aligns the mesh very well with the bow shock which results in minimal smearing of the discontinuity and low oscillations downstream of the shock.

The domain was created as a wedge-shape to model the axisymmetric flow. For the supersonic inlet, the freestream conditions were fixed. The outlet was modeled with a non-reflecting characteristic boundary condition and the sides in circumferential direction were modeled with symmetry boundary conditions. The domain was extended for about 2.5 vehicle lengths downstream of the nozzle exit, which is sufficient in the purely supersonic trailing edge flow. The final 2D-axisymmetric grid was found in a mesh convergence study and had around $300k$ cells, with one cell in circumferential direction. The near-wall mesh was refined to $y^+ < 1$, so no wall model is required.

4. Transient behavior after nozzle start

To investigate the nozzle plume when the vehicle is launched, the staring dynamics of the engine were simulated in stationary external fluid. A non-reflecting farfield boundary condition was applied to all external boundaries of the domain. The nozzle was initialized with the combustion chamber stagnation conditions of $p_0 = 187$ bar, $T_0 = 3058$ K, $\mathrm{Ma} = 0$, and a mass fraction of the exhaust gas of $Y_{\text{exhaust gas}} = 1$. A time series of the Mach number on a slice through the vehicle axis is shown in fig. 4. The pressure jump at the nozzle exit causes a right-running shock wave into the external fluid ($t = 0.04$ ms). Supersonic flow is soon established near the nozzle exit and a Prandtl-Meyer expansion forms around the nozzle lip, which increases the local Mach number further. A second shock forms downstream of the expansion and extends towards the nozzle axis, forming a semicircular shock structure ($t = 0.27$ ms).

After start-up, a left-running expansion accelerates the fluid continuously towards the nozzle exit. Once $\mathrm{Ma} = 1$ is established in the nozzle throat, i.e. the flow is chocked, supersonic expansion further accelerates the fluid in the divergent part of the nozzle. Due to the higher pressure near the nozzle exit, a third shock wave forms and is convected downstream ($t = 0.39$ ms).
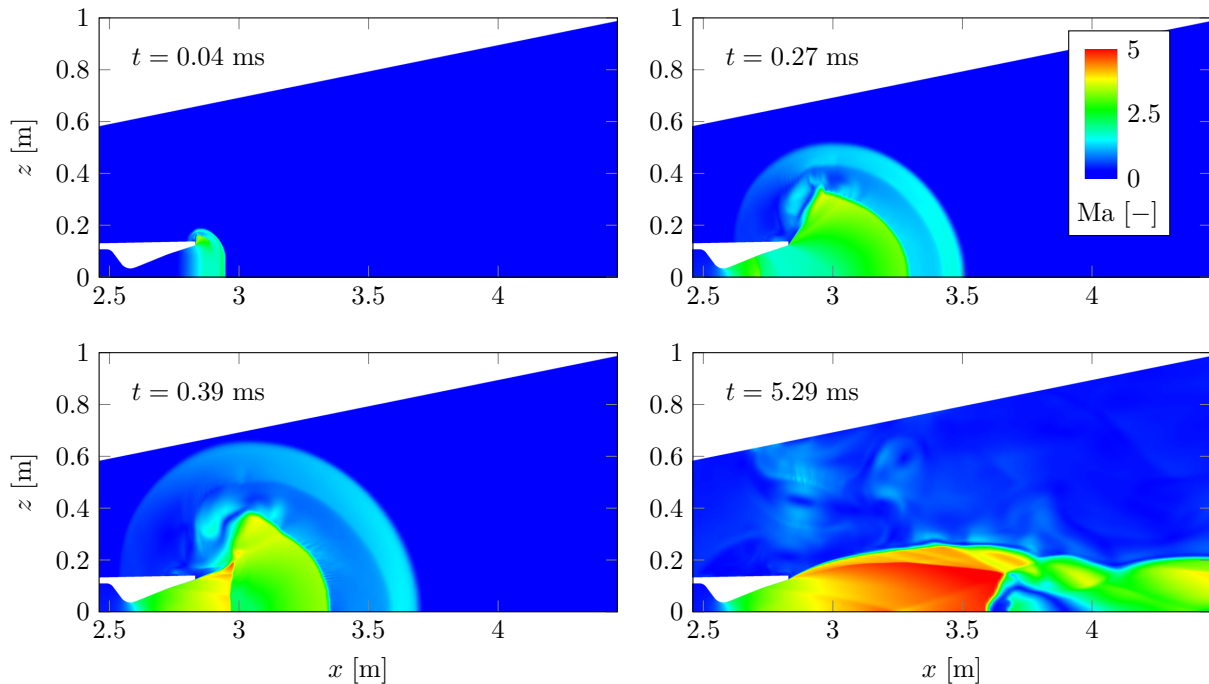
Fig 4. Mach number contours during the transient start-up of the nozzle on a slice through the vehicle axis after initializing the nozzle with combustion chamber stagnation conditions at $t = 0\ ms$.

In the stationary external fluid, no steady state solution could be obtained. The transient behavior after start-up shows strong vortices in the external fluid around the plume. These interact with the nozzle flow and introduce unsteady fluctuations that shift the plume shock structure. These fluctuations can be seen at the timestamp $t = 5.29\ \mathrm{ms}$ in fig. 4.

Steady state solutions were obtained when the supersonic external flow is included, as the upstream influence of perturbations is prevented. The total pressure in the external flow is also significantly higher compared to the stationary case. The nozzle is therefore less over-expanded which appears to improve plume stability.

5.   Nozzle flow interaction with external flow

A complex flow structure is observed at the nozzle lip, when the external fluid is not stationary. Near the rear of the vehicle, the flow outside the boundary layer is nearly at $\mathrm{Ma} = \mathrm{Ma}_\infty$. The Mach number inside the nozzle near the exit ($\mathrm{Ma} \approx 3.3$) is determined by the nozzle area ratio of $\epsilon \approx 3.46$.

Fig. 5a shows a schematic view of the complex flow structure around the nozzle lip of configuration 1, the structures are simplified as straight lines for clarity. Both the internal nozzle flow and the external flow are deflected around the nozzle lip by Prandtl-Meyer expansion fans. The flow is separated near the wall as the corner is too sharp for a smooth deflection. A vortex structure can be seen in this separated area. Fig. 5b shows a Mach number plot of the separated region. Multiple areas with negative axial velocity u are visible.

The internal and external flows are aligned downstream of the Prandtl-Meyer expansions by two shock waves that equalize the internal and external pressure. The external shock wave is referred to as plume shock, the shock propagating towards the jet axis is called barrel shock. Additionally, a contact discontinuity develops between the shock waves, where the nozzle exhaust gas and the external air flow meet with the same flow direction but different thermodynamic states and velocities.

In contrast to the nozzle flow into a stationary surrounding medium, a steady state solution can be obtained at $\mathrm{Ma}_\infty = 7$. The largely supersonic external flow prohibits the upstream propagation of information. The large vortex structures in the stationary external medium are prevented and the
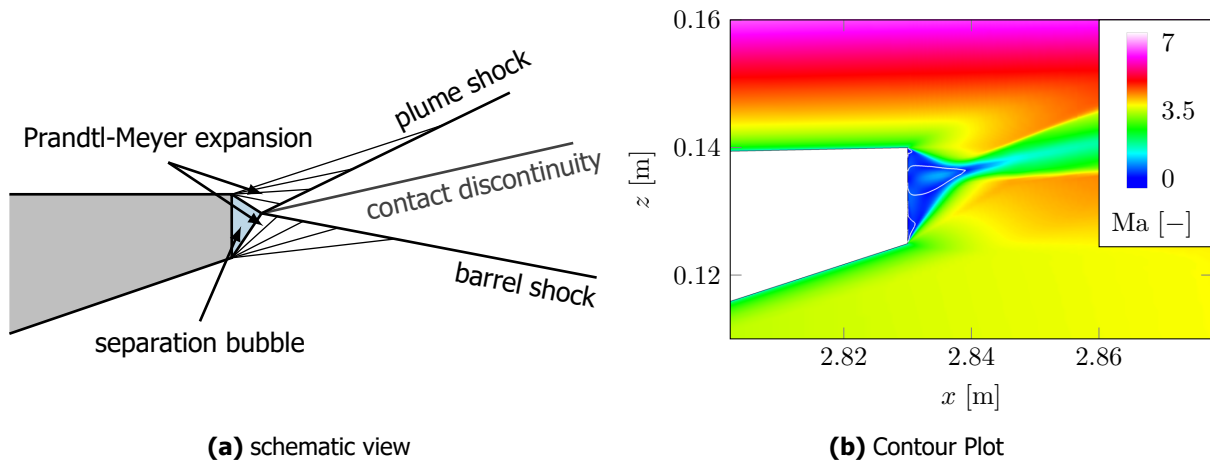
(a) schematic view

(b) Contour Plot

Fig 5. Separation bubble at the nozzle lip. (a) shows a schematic overview of the flow structure. (b) shows a contour plot of the Mach number for $\mathrm{Ma}_\infty = 7$, the outer edge of the separation bubble is indicated by the white line at $u = -10^{-3}\ \mathrm{m/s}$

nozzle plume reaches a steady state. The external flow therefore has a large influence on the plume flow and the form of the separated regions, it most notably seems to stabilize the plume.

To investigate this proposition, multiple simulations were conducted at a range of freestream Mach numbers. Fig. 6 shows the Mach number on a slice through the vehicle axis for the design freestream Mach number $\mathrm{Ma}_\infty = 7$ for the propelled configuration 1 and a non-propelled reference configuration. A strong detached bow shock wave can be seen upstream of the vehicle. The Prandtl-Meyer expansion introduced by the cone angle change at $x \approx 0.73\ \mathrm{m}$ interacts with the bow shock downstream of $x \approx 1.57\ \mathrm{m}$ and decreases the shock angle.

In the non-propelled configuration (see the bottom of fig. 6), a strong Prandtl-Meyer expansion forms at the rear end of the vehicle, which increases the local Mach number to $\mathrm{Ma} > \mathrm{Ma}_\infty$. The flow separates at the sharp rear edge of the vehicle and high negative axial velocities are observed. A re-compression shock forms further downstream. The flow is stable at $\mathrm{Ma}_\infty = 7$ and a steady state solution was found for the separation.

The complex nozzle plume structure can be seen in the top half of fig. 6. A weak oblique shock is triggered by the concave contour change in the nozzle at around $x = 2.72\ \mathrm{m}$. The plume shock and barrel shock, which were shown in fig. 5b, originate from the nozzle lip and propagate into the external flow and the nozzle plume respectively. The barrel shock is reflected at the axis and propagates through the jet boundary. Where it intersects the boundary, it is reflected back towards the center of the jet and a second shock in the external flow forms. The higher Mach number in the external flow results in a smaller shock angle. The expansion from the convex nozzle contour downstream of the nozzle throat also travels through the jet boundary and is partially reflected back towards the axis. The effect is a repeated compression and expansion of both the nozzle jet and the external flow. Fig. 7 shows the same plot for freestream Mach numbers of $\mathrm{Ma}_\infty = 3$ and $\mathrm{Ma}_\infty = 5$, note that the colormap is changed from fig. 6 for better contrast. The overall image is very similar, but the angle of the first bow shock and the plume shock are larger for lower freestream Mach numbers.

Fig. 8 shows the pressure distribution along the vehicle axis for the different freestream Mach numbers. The exhaust gas is expanded in the first part until the oblique shock, originating from the nozzle contour change, impinges on the axis at around $x = 3.27\ \mathrm{m}$. The gas is further expanded until the much stronger oblique shock from the nozzle lip reaches the axis. The total pressure in the external flow increases with the freestream Mach number, this increases the strength and the shock angle of the barrel shock. The shocks therefore reach the axis further upstream for higher Ma_∞. The shocks after the first reflection at the jet boundary reach the axis at around $x = 4.5\ \mathrm{m}$ and are successively weaker at lower Ma_∞.
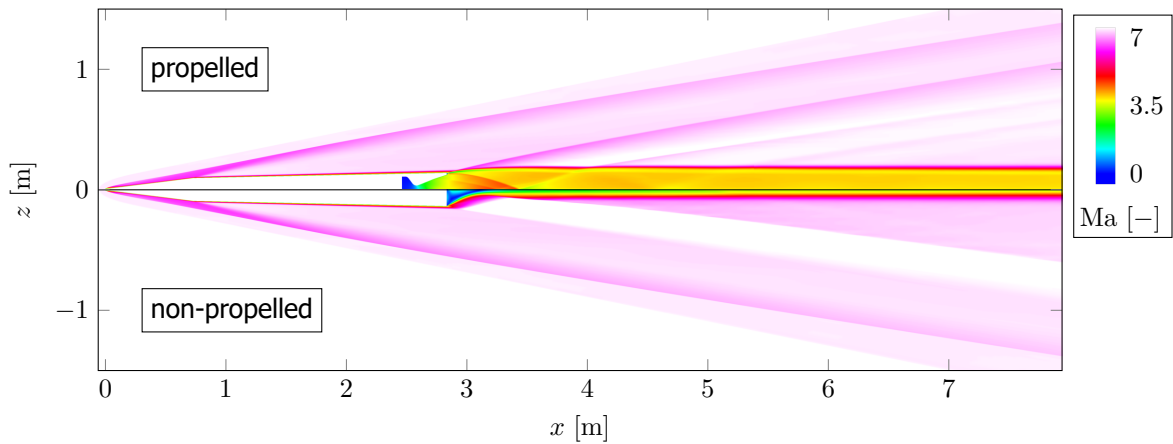
Fig 6. Flow structure around the vehicle at $\mathrm{Ma}_\infty = 7$. The flow around the propelled vehicle is shown in the top half, the bottom half shows a reference configuration without propulsion.
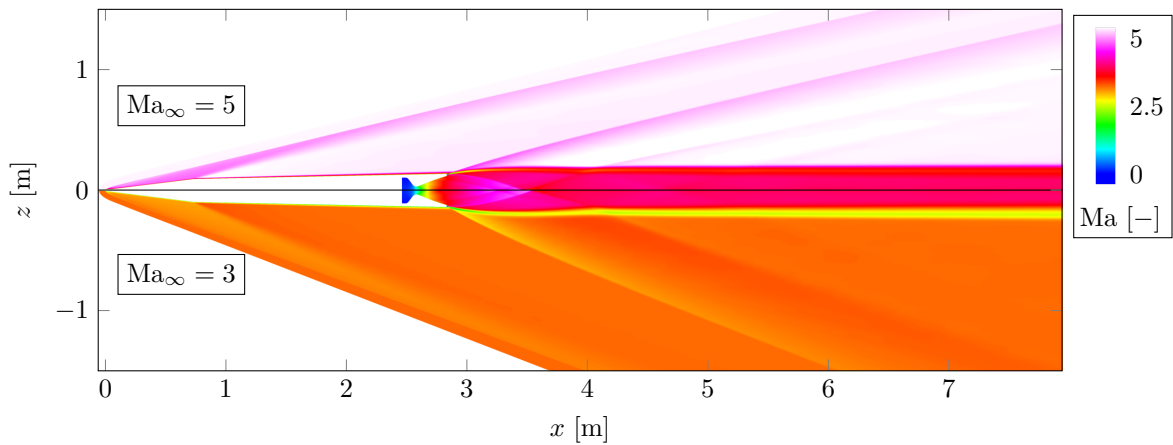

Fig 7. Mach number contour plots for $\mathrm{Ma}_\infty = 3$ and $\mathrm{Ma}_\infty = 5$, note the different colormap to fig. 6
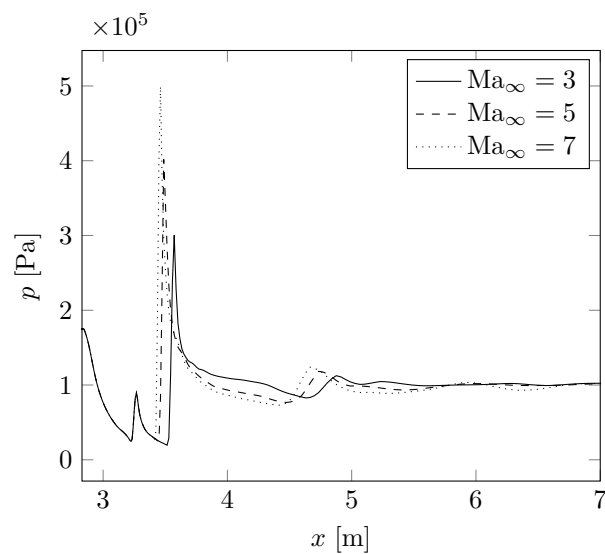

Fig 8. Pressure distribution along the vehicle axis downstream of the nozzle rear.
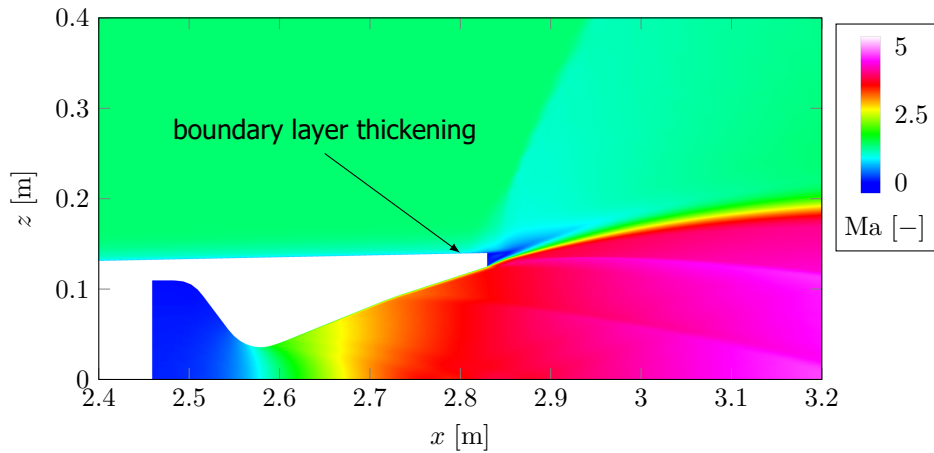
Fig 9. Mach number contour near the nozzle for $\mathrm{Ma}_\infty = 1.3$ after the transient fluctuations dissipate.

As shown, the plume gets wider with a lower freestream Mach number and the angle of the plume shock increases. This affects the shape of the separation bubble at the nozzle rim. Below a certain freestream Mach number, the plume shock induces a thickening of the boundary layer near the nozzle rim. Due to that, the shock transitions to a gradual compression near the wall.

Simulations were performed with a low supersonic freestream Mach number of $\mathrm{Ma}_\infty = 1.3$, where this transition occurred. A noticeable thickening of the boundary layer can be seen downstream of $x = 2.8$ m in fig. 9. Steady state simulations using local time-stepping failed to converge, likely due to the sensitivity of the shock wave/boundary layer interaction. Therefore, transient simulations with global time-stepping were performed until a steady state was reached. The outer part of the plume shock has a large shock angle, the Prandtl-Meyer expansions around the nozzle rim is much weaker. Compared to the case with $\mathrm{Ma}_\infty = 7$ (fig. 5b), the length of the separated region at the nozzle rim is increased.

A large flow separation is visible for configuration 2 at the cavity on the outside of the nozzle, see fig. 11. The density gradient in x direction $\partial \rho / \partial x$ is shown for $\mathrm{Ma}_\infty = 7$, the yellow line marks $\mathrm{Ma} = 1$. The external flow is redirected towards the nozzle outer nozzle wall with a Prandtl-Meyer expansion. Due to the right angle at the vehicle rear, the flow separates and a large subsonic recirculation zone forms. A strong shock wave forms on the outside of the nozzle to align the flow with the diverging outer nozzle wall. Compared to configuration 1, the fluid leaves the nozzle parallel to the external flow. The flow around the nozzle lip still consists of the same shock structure shown in 5a, but the plume shock is significantly weaker because the change in flow direction is smaller compared to configuration 1. Figure 10 shows the Mach number contour for configuration 2 at freestream Mach numbers $\mathrm{Ma}_\infty = 3$ and $\mathrm{Ma}_\infty = 5$. The expansion upstream of the plume shock and the separated regions are visible. The maximum deflection angle of a Prandtl-Meyer expansion increases with Mach number. This is especially noticeable at $\mathrm{Ma}_\infty = 3$, where the separation extends to the nozzle rim.

Figure 12 shows the radial distribution of the axial velocity component u for both configurations at $\mathrm{Ma}_\infty = 3, 5$, and 7. It shows a slight increase of plume core velocity with external Mach number. The core velocity is also slightly higher for configuration 2 due to the weaker barrel shock. Configuration 2 also shows lower local minimum at $z \approx \pm 0.2$ m, which stems from the low speed flow in the cavity outside the nozzle. The difference in the nozzle plume can only be observed downstream of the nozzle exit, where the external flow impacts the plume. Inside the nozzle, the flow conditions are the same for all cases due to the supersonic flow.
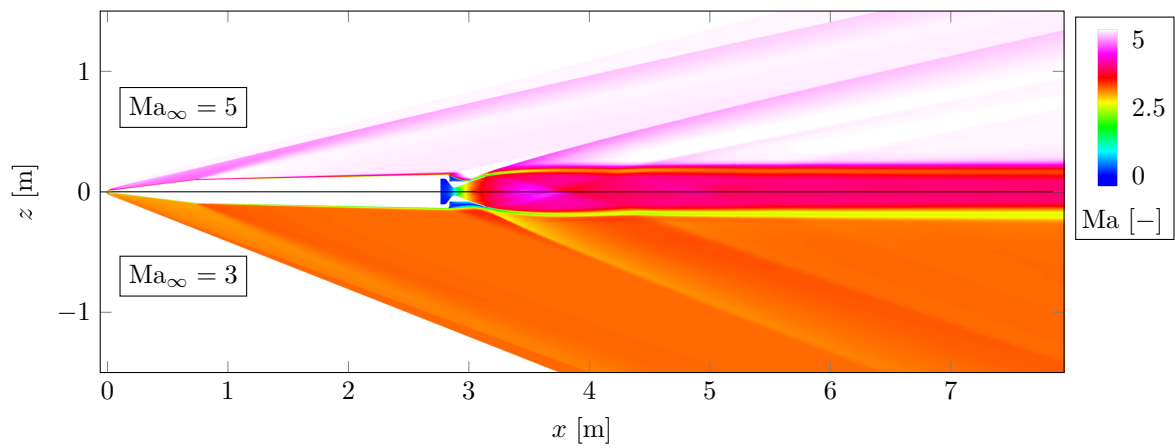
Fig 10. Mach number distribution for configuration 2 at $Ma_\infty = 3$ and $Ma_\infty = 5$.
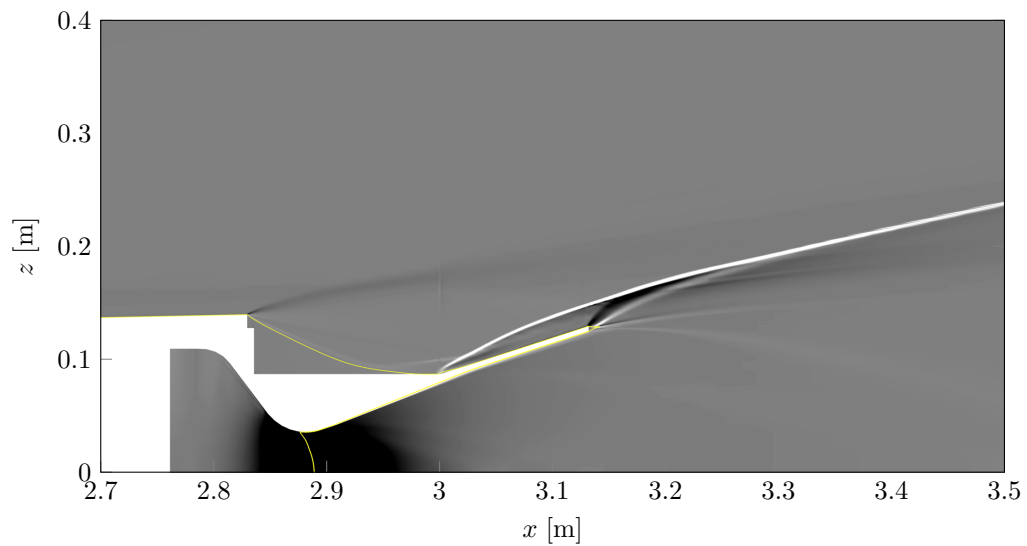

Fig 11. Numerical schlieren image of the cavity for configuration 2 at $Ma_\infty = 7$, $\partial \rho / \partial x$ is shown, the yellow line marks $Ma = 1$.
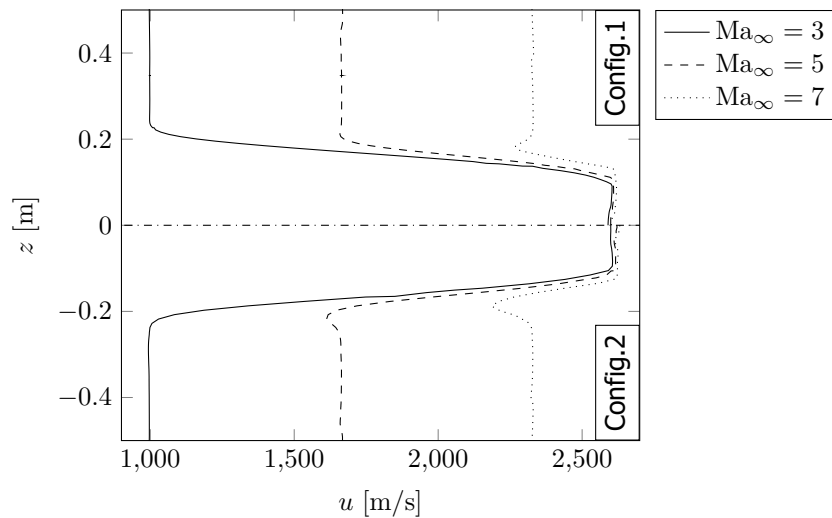
Fig 12. Radial velocity distribution 10 nozzle exit diameters behind the vehicle.

6. Nozzle plume stability

The nozzle flow and its interaction with the external flow has a significant impact on the stability of the vehicle. In the previous section, two different physical effects that can affect vehicle stability were found.

In configuration 1 the plume shock causes a boundary layer separation on the outside of the vehicle rear. Because this separation develops freely and is not triggered by a distinct geometry change, it can be very sensitive to external disturbances. In flight, especially when an angle of attack is introduced, this is expected to produce asymmetric separation and the vehicle could experience large lateral forces.

The nozzle plume of configuration 1 seems to be more susceptible to flow instability for lower Ma_∞, as no stable steady-state solution could be obtained for $\mathrm{Ma}_\infty = 0$ and the $\mathrm{Ma}_\infty = 1.3$ case failed to converge with local time-stepping. Kelvin-Helmholtz-like instabilities occur at the shear layer between the plume and the external flow. This seems to be in contrast to the literature findings by Karimi and Girimaji [18], who show that Kelvin-Helmholtz instability is suppressed at higher velocity differences of planar shear layers.
The axisymmetric case in this publication appears to exhibit opposing behavior. One possible explanation is that the relative magnitude of velocity perturbations in the external flow reduce as the external flow speed is increased. The higher inertia of the external flow could then stabilize the flow against oscillations.

As seen, configuration 2 shows a large separation on the outside of the nozzle even in hypersonic flight at $\mathrm{Ma}_\infty = 7$. This could also lead to significant lateral forces when the separation becomes asymmetrical. However, the increased vehicle length and high pressure on the outer nozzle wall also affect the pressure center. For configuration 1, the pressure center is at $x = 2.48$ m, for configuration 2, it is at around $x = 2.78$ m. Assuming the center of gravity of the vehicle is constant, configuration 2 has a higher longitudinal stability, but is more susceptible to transient instability effects.

When running the $\mathrm{Ma}_\infty = 7$ cases without turbulence, a steady-state solution could only be found for configuration 1. In configuration 2, the flow separates completely at the edge of cavity, which creates a separation bubble that spans the entire nozzle section up to the nozzle rim. The shape of the bubble fluctuates over time, generating weak shocks in the external flow.

7. Conclusion

The interaction of a hypersonic external flow with the nozzle plume of a generic hypersonic vehicle in dense atmosphere was investigated numerically. Focus was placed on modeling the relevant chemical

reaction effects in the fluid with a reasonable computational effort. The nozzle exhaust gas was modeled as a perfect gas with the effective ratio of specific heats after combustion, as the influence of chemistry on the relevant fluid properties is minor. Future investigations could compare more sophisticated thermodynamic models of the exhaust gas with the ideal gas assumption.

It was shown that the nozzle flow is stable during hypersonic flight for configuration 1 but generates a separated boundary layer near the nozzle lip for low supersonic speeds. This is a potential risk for the vehicle stability. The same transition can be observed at high altitudes due to increasing nozzle under-expansion but it is seen here, that a decrease in freestream Mach number produces a similar effect, even though the static pressure in both the nozzle and the freestream are constant.

Configuration 2 shows a large separation due to its geometry that could potentially produce flow instability. Any cavities should therefore be avoided for the most stable flight configuration.

References

1. Hadjadj, A., Onofri, M.: Nozzle flow separation. In: Shock Waves 19.3 (2009), pp. 163–169. ISSN: 0938-1287. DOI: 10.1007/s00193-009-0209-7.

2. Frey, M.: Shock Patterns in the Plume of Overexpanded Rocket Nozzles. In: Aerothermodynamics for space vehicles. Ed. by Harris, R. A. ESTEC, Noordwijk, The Netherlands, 1999.

3. Castner, R. S., Elmiligui, A., Cliff, S.: Exhaust Nozzle Plume and Shock Wave Interaction. In: 51st Aerospace Science Conference. Grapevine, Texas: American Institute of Aeronautics and Astronautics, 2013.

4. Raghunathan, S., Kim, H., Benard, E., Mallon, P., Harrison, R.: Plume Interference Effects On Missile Bodies. In: 39th Aerospace Sciences Meeting and Exhibit. Reno, NV: American Institute of Aeronautics and Astronautics, 2001, 59E. DOI: 10.2514/6.2001-259.

5. Alpinieri, L. J., Adams, R. H.: Flow Separation Due to Jet Pluming. In: AIAA Journal 4.10 (1966), pp. 1865–1866. ISSN: 0001-1452. DOI: 10.2514/3.3802.

6. Desikan, S. L. N., Suresh, K., Saravanan, R., Patil, M. M., Balasubramanian, P., Prasath, M.: Effect of Freestream–Plume Interaction on Launch Vehicle Aerodynamics. In: Journal of Spacecraft and Rockets 53.2 (2016), pp. 354–369. ISSN: 0022-4650. DOI: 10.2514/1.A33413.

7. Leyland, P., Vos, J., van Kemenade, V., Ytterstrom, A.: NSMB - A Modular Navier Stokes Multiblock Code for CFD. In: 33rd Aerospace Sciences Meeting and Exhibit. Reno, NV: American Institute of Aeronautics and Astronautics, 1995, p. 2867. DOI: 10.2514/6.1995-568.

8. Wilcox, D. C.: Turbulence modeling for CFD. Third edition. La Cañada, California: DCW Industries, 2006. ISBN: 978-1-928729-08-2.

9. Buck, A., Mundt, Ch.: On RANS Turbulence Models for High-Speed Applications. In: AIAA Scitech 2021 Forum. VIRTUAL EVENT: American Institute of Aeronautics and Astronautics, 2021. ISBN: 978-1-62410-609-5. DOI: 10.2514/6.2021-1744.

10. Liou, M.-S.: A Sequel to AUSM: AUSM+. In: Journal of Computational Physics 129.2 (1996), pp. 364–382. ISSN: 00219991. DOI: 10.1006/jcph.1996.0256.

11. Yoon, S., Jameson, A.: A Multigrid LU-SSOR Scheme for Approximate Newton Iteration Applied to the Euler Equations. 1986.

12. Williamson, J.: Low-storage Runge-Kutta schemes. In: Journal of Computational Physics 35.1 (1980), pp. 48–56. ISSN: 00219991. DOI: 10.1016/0021-9991(80)90033-9.

13. Scoggins, J. B., Magin, T. E.: Development of Mutation++: MUlticomponent Thermodynamic and Transport properties for IONized gases library in C++. In: 11th AIAA/ASME Joint Thermophysics and Heat Transfer Conference. Atlanta, GA: American Institute of Aeronautics and Astronautics, 2014, p1. ISBN: 978-1-62410-281-3. DOI: 10.2514/6.2014-2966.

14. Park, C., Jaffe, R. L., Partridge, H.: Chemical-Kinetic Parameters of Hyperbolic Earth Entry. In: Journal of Thermophysics and Heat Transfer 15.1 (2001), pp. 76–90. ISSN: 0887-8722. DOI: 10.2514/2.6582.

15. Sutton, G. P., Biblarz, O.: Rocket Propulsion Elements: An introduction to the engineering of rockets. 7th ed. New York: John Wiley & Sons, 2000. ISBN: 0-471-32642-9.

16. Gordon, S., McBride, B. J.: Computer Program for Calculation of Complex Chemical Equilibrium Compositions and Applications: I. Analysis. In: NASA Reference Publication 1331 (1994).

17. Klaimon, J. H.: Bow Shock Correlation for Slightly Blunted Cones. In: AIAA Journal 1.2 (1963), pp. 490–491. ISSN: 0001-1452. DOI: 10.2514/3.1581.

18. Karimi, M., Girimaji, S. S.: Suppression mechanism of Kelvin-Helmholtz instability in compressible fluid flows. In: Physical review. E 93 (2016), p. 041102. DOI: 10.1103/PhysRevE.93.041102.